Volume 16
Number 43
21 November 2025
Pages 20089–20616

Chemical Science

rsc.li/chemical-science

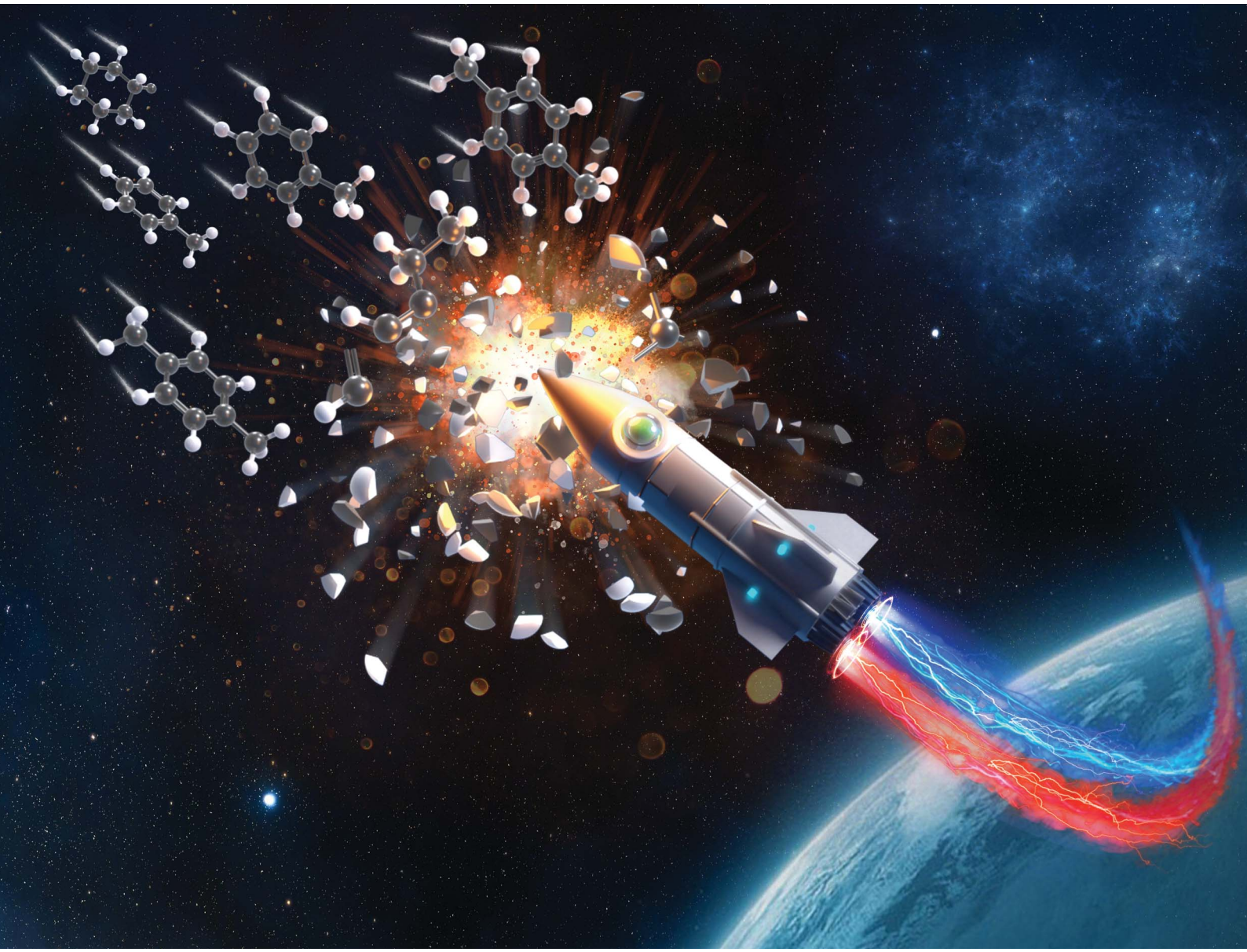

ISSN 2041-6539

ROYAL SOCIETY OF CHEMISTRY

EDGE ARTICLE

Chi Zhang, Ke Hu *et al.*

Two-step coupled photoelectrochemical chlorination and oxygenation of C(sp^3)–H bonds mediated by chlorine radicals over a modified $BiVO_4$ photoanode

15 YEARS ANNIVERSARY

Chemical Science

ROYAL SOCIETY OF CHEMISTRY

EDGE ARTICLE

View Article Online
View Journal | View Issue

Cite this: *Chem. Sci.*, 2025, **16**, 20229

All publication charges for this article have been paid for by the Royal Society of Chemistry

Two-step coupled photoelectrochemical chlorination and oxygenation of C(sp^3)–H bonds mediated by chlorine radicals over a modified $BiVO_4$ photoanode

Weijian Yang,[a] Pengju Li,[a] Yiming Han,[a] Zijian Zhao,[a] Limei Tian,[a] Zhenghao Zhang,[a] Mark G. Humphrey,[c] Chi Zhang *[b] and Ke Hu *[ab]

Photoelectrochemical (PEC) cells are emerging tools for fine chemical synthesis, but often suffer from low solar-to-product conversion efficiency, especially in energy-demanding reactant activation. Herein, we report chlorination and oxygenation of energy-demanding C(sp^3)–H bonds using a two-step coupled PEC cell, avoiding the direct generation of high-energy chlorine radicals (Cl$^\bullet$). The photoanode consists of a $BiVO_4$ semiconductor modified with TiO_2 and a $CoNi_2O_x$ chlorine evolution reaction (CER) catalyst. Under 1 sun illumination, the $BiVO_4/TiO_2/CoNi_2O_x$ photoanode showed a photocurrent density of 2.9 mA cm^{-2} for CER at 0.8 V *vs.* the reversible hydrogen electrode (RHE) with the highest applied bias photon-to-current efficiency of 3.20%. Subsequent homolysis of Cl_2 under white light generates Cl$^\bullet$, activating C(sp^3)–H bonds following hydrogen atom transfer. The PEC cell selectively chlorinated hydrocarbons under argon, and enabled oxygenation to afford aldehydes, ketones, and alcohols when the atmosphere was switched to dioxygen, offering a green and efficient synthetic approach. Studies on the reaction mechanism revealed that Cl$^\bullet$ is the key reactive intermediate responsible for C(sp^3)–H bonds activation. This work offers a solar-driven energy-efficient strategy for the generation of Cl$^\bullet$ from chloride salts and activation of energy-demanding C(sp^3)–H bonds, highlighting its great potential in advancing green chemical synthesis.

Received 12th July 2025
Accepted 9th September 2025

DOI: 10.1039/d5sc05195a

rsc.li/chemical-science

Introduction

The activation and functionalization of inert C(sp^3)–H bonds are essential goals in synthetic organic chemistry, with significant implications for fine chemical production.[1–4] Traditional methods for C(sp^3)–H activation, such as chlorination and oxygenation, often require external oxidants (*e.g.*, 2-iodoxybenzoic acid,[5,6] S_2O_8,[2–7] *etc.*), hazardous reagents (*e.g.*, Cl_2,[8] *N*-chlorosuccinimide,[9,10] NaClO,[11] *etc.*), expensive metal-based catalysts (*e.g.*, Au,[12] Rh,[13] Pd,[14] *etc.*), and harsh reaction conditions (*e.g.*, elevated temperature and pressure,[15] *etc.*). These challenges limit their application in green and sustainable chemistry (Scheme 1).

Photoelectrochemical (PEC) cells, which use sunlight to drive chemical reactions, offer a promising alternative to conventional methods, as they enable chemical transformations under milder conditions.[16–22] PEC synthesis has been successfully applied to form C–N,[23] C–O,[24,25] C–P,[26] and C–X[27] bonds *via* C–H functionalization.[28–31] However, the direct activation of C(sp^3)–H bonds, especially those in alkanes with bond dissociation energies (BDE) of approximately 96–101 kcal mol^{-1}, remains difficult in PEC systems due to their

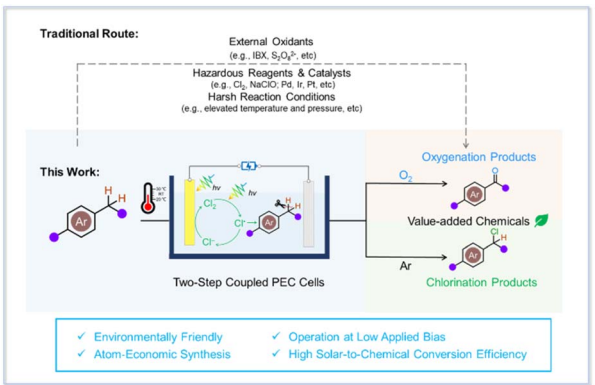

Scheme 1 C(sp^3)–H bond chlorination and oxygenation driven by traditional routes and by the two-step coupled PEC approach in this work.

[a]*Department of Chemistry and Shanghai Key Laboratory of Molecular Catalysis and Innovative Materials, Fudan University, 220 Handan Road, Shanghai 200433, P. R. China. E-mail: khu@fudan.edu.cn*

[b]*School of Chemical Science and Engineering, Tongji University, 1239 Siping Road, Shanghai 200092, P. R. China. E-mail: chizhang@tongji.edu.cn; khu@tongji.edu.cn*

[c]*Research School of Chemistry, Australian National University, Canberra, ACT 2601, Australia*

high activation energy.[32,33] One promising approach to overcome these challenges is the use of redox mediators that facilitate hydrogen atom transfer (HAT).[32,34–40] The chlorine radical ($Cl^{\bullet}$) is particularly effective as a HAT mediator, because it is capable of abstracting hydrogen atoms from hydrocarbons to form carbon-centered radicals.[27,41–46] While the generation of $Cl^{\bullet}$ from one electron oxidation of Cl^{-} is energy-demanding and requires a high reduction potential ($E°(Cl^{\bullet}/Cl^{-}) = 2.2–2.4$ V *vs.* normal hydrogen electrode (NHE) in aqueous solutions[47,48]), this challenge can in principle be mitigated through a two-step coupled photoelectrochemical process.

In this work, we propose a novel two-step coupled PEC process for generating $Cl^{\bullet}$ from Cl^{-}. The principle is straightforward: since the one-electron oxidation of Cl^{-} in aqueous solution is highly energy-demanding, we design the photoanode to intentionally facilitate a two-electron oxidation of Cl^{-} to Cl_2 through photoelectrocatalysis first ($E°(Cl_2/Cl^{-}) = 1.48$ V *vs.* RHE).[47] Cl_2 in the aqueous phase diffuses away from the photoanode and to the organic phase where $Cl^{\bullet}$ is then photogenerated through the homolysis of Cl_2 in the second step. Importantly, our mechanistic study found that $Cl^{\bullet}$ intermediate in the second step, rather than other chlorine species like Cl_2 or dichloride radical anion ($Cl_2^{\bullet-}$),[49] plays a crucial role in the PEC cell. This design of merging photoelectrocatalysis and photocatalysis/photolysis is inspired by the *Z*-scheme of natural photosynthesis, where the production of highly reducing NADPH equivalents and oxygen evolution is spatially separated across two photosystems and the electron transport chain. Therefore, two redox-difficult reactions can proceed at relatively high efficiency under mild conditions.[50,51] This two-step coupled approach allows for the activation of energy-demanding $C(sp^3)$–H bonds with readily available NaCl aqueous solution in a PEC cell, avoiding the need for toxic reagents or organic chloride sources (Scheme 1).

Results and discussion

Design and characterization of the modified $BiVO_4$ photoanode

Monoclinic $BiVO_4$ photoanodes were prepared according to prior reports with minor modifications.[52,53] To synthesize the $BiVO_4/TiO_2/CoNi_2O_x$ photoanode, a protective TiO_2 overlayer[54] was deposited onto the surface of $BiVO_4$ through atomic layer deposition (ALD). Then, $CoNi_2O_x$ was decorated on the $BiVO_4/TiO_2$ surface as a CER catalyst[55] by drop casting (Fig. 1a). The structural and morphological properties of the resulting $BiVO_4/TiO_2/CoNi_2O_x$ photoanode were first analyzed using X-ray diffraction (XRD) and high-resolution transmission electron microscopy (HRTEM). XRD revealed the presence of monoclinic $BiVO_4$ peaks, confirming the preservation of the crystal structure after modifications (Fig. S1). HRTEM analysis showed that the TiO_2 overlayer had a uniform thickness of ~4.4 nm on the $BiVO_4$ surface (Fig. 1b). The $CoNi_2O_x$ catalyst displayed a nanosheet-type morphology with polygonal shapes and widths ranging from 100–400 nm (Fig. S3). X-ray photo-electron spectroscopy (XPS) confirmed the presence of Ni^{2+}/Ni^{3+} and Co^{2+}/Co^{3+} species (Fig. S2). Scanning electron microscopy (SEM)

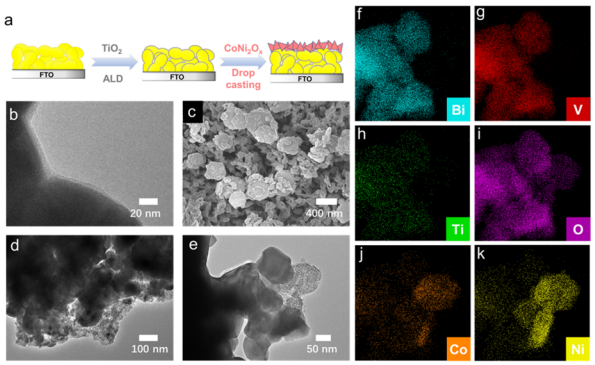

Fig. 1 (a) Schematic illustration of the construction of the $BiVO_4/TiO_2/CoNi_2O_x$ photoanode. (b) HRTEM image of $BiVO_4/TiO_2$. (c) SEM image of $BiVO_4/TiO_2/CoNi_2O_x$. (d and e) HRTEM images of $BiVO_4/TiO_2/CoNi_2O_x$. (f–k) STEM-EDS maps showing the distribution of Bi, V, Ti, O, Co, and Ni in $BiVO_4/TiO_2/CoNi_2O_x$.

further illustrated the successful loading of $CoNi_2O_x$ onto the $BiVO_4/TiO_2$ surface (Fig. 1c), with close attachment of the nanosheets to the photoanode (Fig. 1d and e). The presence of Bi, V, Ti, O, Co and Ni in the $BiVO_4/TiO_2/CoNi_2O_x$ photoanode (Fig. 1f–k) was confirmed using scanning transmission electron microscopy-energy dispersive X-ray spectroscopy (STEM-EDS) with a Co/Ni ratio of 1 : 2 (Fig. S4 and Table S1).

The PEC performance of different photoanodes for CER was first evaluated using linear sweep voltammetry (LSV). As illustrated in Fig. 2a, $BiVO_4$ showed a low photocurrent density of 1.2 mA cm^{-2} at 1.2 V *vs.* the reversible hydrogen electrode (RHE) under AM 1.5G illumination (100 mW cm^{-2}). Fortunately, the photocurrent density was significantly enhanced by the addition of TiO_2 or $CoNi_2O_x$, reaching 2.1 mA cm^{-2} and 3.0 mA cm^{-2} for $BiVO_4/TiO_2$ and $BiVO_4/CoNi_2O_x$, respectively. It is worth noting that the thickness of the TiO_2 overlayer can influence the PEC performance of $BiVO_4/TiO_2$; the optimal thickness for CER was found to be ~4.4 nm (Fig. S5). The Co/Ni ratio of the CER catalyst also has a significant influence on the overall performance (Fig. S6a and b). The optimized photoanode composition is $BiVO4/TiO_2/CoNi_2O_x$, exhibiting a remarkable photocurrent density of 2.9 mA cm^{-2} at 0.8 V *vs.* RHE and 5.4 mA cm^{-2} at 1.2 V *vs.* RHE (Fig. 2a). However, when we excluded the $BiVO_4$ layer from the $BiVO_4/TiO_2/CoNi_2O_x$ architecture, *i.e.* $TiO_2/CoNi_2O_x$ that had no visible-light absorption, no photocurrent was generated, confirming the critical role of $BiVO_4$ as the primary light-absorbing unit. Additionally, the incident photon-to-current conversion efficiency (IPCE) of different photoanodes revealed that the $BiVO_4/TiO_2/CoNi_2O_x$ displayed excellent IPCE values above 80% from 400 to 450 nm (Fig. 2b), consistent with its outstanding PEC performance for CER. Other photoanode configurations showed much lower IPCE values within the same wavelength range.

Intensity modulated photocurrent spectroscopy (IMPS) characterizations were carried out to probe the hole transfer kinetics of photoanodes from bulk to surface. The charge transfer rate constant (k_{tr}) and charge recombination rate constant (k_{rec}) were determined from the IMPS spectra (Fig. S7a

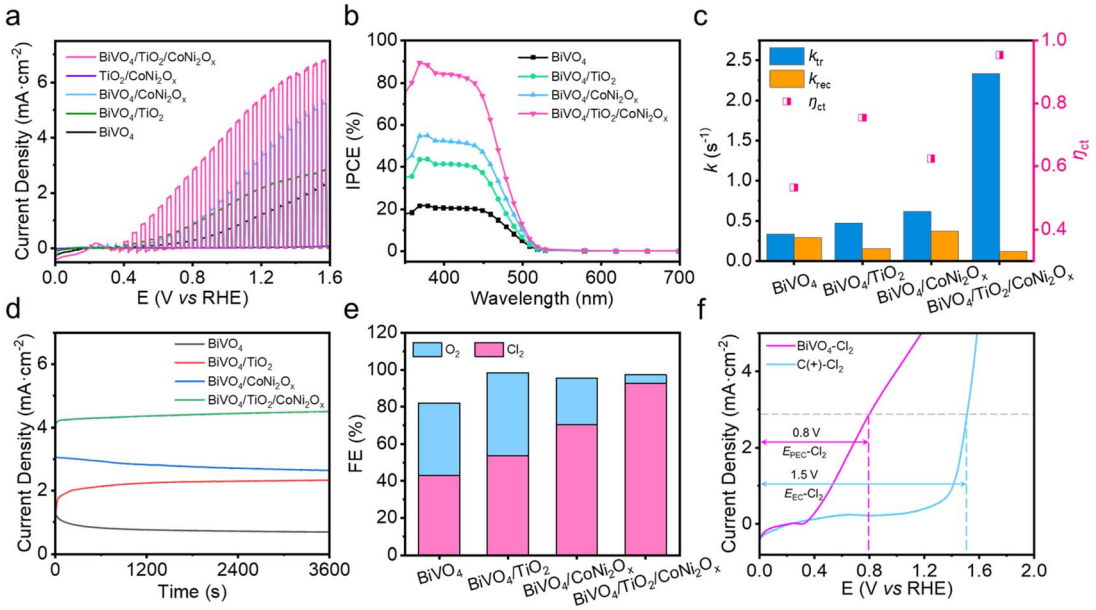

Fig. 2 (a) Chopped LSV curves of different photoanodes in 0.5 M NaCl solution (pH = 2) under AM 1.5G light illumination (100 mW cm^{-2}). (b) IPCE spectra of the different photoanodes at 1.2 V *vs.* RHE. (c) Plot of k_{tr}, k_{rec}, and η_{ct} values calculated from the IMPS measurements for different photoanodes. (d) *J*–t curves for long-term PEC CER tests of different photoanodes in 0.5 M NaCl (pH = 2) aqueous solution at 1.2 V *vs.* RHE. (e) FE values of various photoanodes for Cl_2 and O_2 evolution. Reaction time: 1 h. (f) Current density from PEC using modified $BiVO_4$ photoanode as a function of E_{app} and comparison with electrochemical (EC) oxidation of Cl^- to Cl_2. The vertical dashed lines represent the E_{app} needed for the two oxidation processes when the current density at each indicated (photo)electrode reaches 2.9 mA cm^{-2}.

and b).[56] The k_{tr} and k_{rec} values of various photoanodes are shown in Fig. 2c. $BiVO_4$ displayed a k_{rec} value of 0.29 s^{-1} along with a k_{tr} value of 0.33 s^{-1}. For $BiVO_4/TiO_2$, the TiO_2 overlayer slowed down the charge recombination and enhanced the hole transfer with $k_{rec} = 0.15$ s^{-1} and $k_{tr} = 0.47$ s^{-1}, indicating its role as a hole transport layer. Meanwhile, the $BiVO_4/CoNi_2O_x$ photoanode showed slightly larger k_{rec} and k_{tr} than $BiVO_4$. For the $BiVO_4/TiO_2/CoNi_2O_x$ photoanode, k_{tr} is about 20-fold higher than k_{rec} (2.34 s^{-1} *vs.* 0.12 s^{-1}). The charge transfer efficiency (η_{ct}) calculated from the k_{rec} and k_{tr} values [$\eta_{ct} = k_{tr}/(k_{rec} + k_{tr}) \times 100\%$] is over 95%, implying almost quantitative charge separation at the photoanode surface (Fig. 2c and Table S2). The charge transport from photoanode surface to electrolyte was investigated by electrochemical impedance spectroscopy (EIS). The EIS spectra collected from different photoanodes fit well with Randle's equivalent circuit (Fig. S8). In this model, lower charge transfer resistance (R_{ct}) indicates faster hole transfer from photoanode surface to electrolyte.[57,58] $BiVO_4/TiO_2/CoNi_2O_x$ photoanode had the lowest R_{ct} among all tested configurations, further confirming the enhancement in charge separation and transfer efficiency at the photoanode-electrolyte interface shown in Table S3.

We also observed that modifying $BiVO_4$ with TiO_2 could improve the photoanode stability. $BiVO_4$ showed poor stability at 1.2 V *vs.* RHE after 1 h of PEC Cl_2 production, with the photocurrent density decreasing from 1.3 mA cm^{-2} to 0.7 mA cm^{-2}. In contrast, $BiVO_4/TiO_2$ and $BiVO_4/TiO_2/CoNi_2O_x$ displayed much better stability, demonstrated the other role of TiO_2 as a protective overlayer (Fig. 2d). Next, we quantified the faradaic efficiency for the CER (FE_{CER}) of the different photoanodes using the *N*,*N*-diethyl-*p*-phenylenediamine (DPD) colorimetric method. The amount of dioxygen byproduct from water oxidation was determined by gas chromatography (GC). The FE_{CER} values for bare $BiVO_4$ (43%) and $BiVO_4/TiO_2$ (54%) were enhanced by the deposition of $CoNi_2O_x$ on $BiVO_4/TiO_2$ (94% for $BiVO_4/TiO_2/CoNi_2O_x$, Fig. 2e). The incorporation of $CoNi_2O_x$ significantly enhanced the FE_{CER} while suppressing oxygen evolution, indicating its role as a CER catalyst. When we deposited $CoNi_2O_x$ or TiO_2 on the FTO substrates and tested their LSV curves (Fig. S9), we found that FTO/$CoNi_2O_x$ exhibited a significant catalytic current compared to FTO and FTO/TiO_2, showing increased current density and reduced onset potential. This indicates the role of $CoNi_2O_x$ as a CER catalyst as well. For the long-term CER test (24 h), an acceptable FE_{CER} above 80% was obtained and an outstanding photocurrent density above 3.0 mA cm^{-2} was maintained for 24 h at 0.8 V *vs.* RHE using $BiVO_4/TiO_2/CoNi_2O_x$ photoanode (Fig. S10). With the systematic testing for each component of the modified photoelectrode, we summarize that $BiVO_4$ acts as the light-absorbing unit; the TiO_2 overlayer serves as the hole transport and protective layer, enhancing charge transfer efficiency and protecting electrode materials; and $CoNi_2O_x$ primarily functions as the CER catalyst, enhancing FE_{CER}. The three components synergistically operate together to achieve the optimized performance.

Fig. 2f illustrates the advantages of the PEC method for CER by plotting the CER current density as a function of the applied potential (E_{app}). The onset potential for Cl_2 evolution at the $BiVO_4/TiO_2/CoNi_2O_x$ photoanode was around 1 V less than that at a carbon electrode. The significantly lower E_{app} for the PEC method (0.8 V *vs.* RHE) compared to electrochemical oxidation

(~1.5 V *vs.* RHE) is crucial. This reduced E_{app} critically lowers the overall cell voltage (E_{cell}) requirement. Significantly, E_{cell} below 1.48 V, corresponding to the thermodynamic potential difference of $E°(Cl_2/Cl^-)$ and $E°(H^+/H_2)$ under our experimental conditions, enables solar energy harvesting for subsequent organic synthesis as quantified by the applied bias photon-to-current efficiency (ABPE) being a positive value (*vide infra*). This enables C(sp^3)–H bond activation initiated by $Cl^•$ under a low E_{app} using the PEC method.

Finally, the efficiency of using the incident light in photoelectrochemical conversion by the $BiVO_4/TiO_2/CoNi_2O_x$-based PEC cell was evaluated by ABPE (eqn (1)),[59]

$$\text{ABPE}\ (\%) = \frac{(E° - E_{cell}) \times J_p}{P_{AM\ 1.5G}} \times 100\% \quad (1)$$

where $P_{AM\ 1.5G}$ is the incident light intensity (100 mW cm^{-2} for AM 1.5G illumination), J_p is the photocurrent density, E_{cell} is the cell voltage between the working electrode and counter electrode (Pt), and $E°$ represents the thermodynamic potential of the cell reaction ($E°(Cl_2/Cl^-) - E°(H^+/H_2)$), which is 1.48 V under our experimental conditions.[47] An outstanding ABPE value of 3.20% was obtained with the $BiVO_4/TiO_2/CoNi_2O_x$ photoanode at 0.8 V, which is 10 times higher than that with bare $BiVO_4$ (Fig. S11). Through this new strategy of Cl_2 production by PEC, we have greatly reduced the E_{app} from values up to 1.5 V *vs.* RHE in electrochemical Cl_2 generation to 0.8 V *vs.* RHE while ensuring efficient Cl_2 evolution.

Photoelectrochemical chlorination of C(sp^3)–H bonds

The PEC chlorination of the C(sp^3)–H bonds was conducted in 30 mL 0.5 M NaCl (pH = 2) solution using cyclohexane as the model substrate. E_{app} of 0.8 V *vs.* RHE was applied to different photoanodes for PEC chlorination tests with 2 mL cyclohexane. After 2 h, the chlorinated products were quantified using GC (Fig. S13a–c) and thus the FE toward the chlorinated products was obtained. Among the different photoanodes, $BiVO_4/TiO_2/CoNi_2O_x$ displayed the highest production rate of 51.5 μmol cm^{-2} h^{-1} toward chlorocyclohexane with a FE of 93% for chlorinated products (Fig. 3a and Table 1, entry 1). For the chlorination of 0.15 mmol (16.2 μL) cyclohexane over $BiVO_4/TiO_2/CoNi_2O_x$, a high yield of 93% for chlorocyclohexane was obtained with white light irradiation (100 mW cm^{-2}) after 10 h (Fig. 3b). However, the decreased initial substrate loading significantly compromised FE. To maintain practical FE, we employed milliliter-scale substrate quantities (>10 mmol) for other compounds, though complete conversion would require impractically long reaction times (>200 h). This trade-off led us to prioritize reporting faradaic efficiencies and product selectivity data.

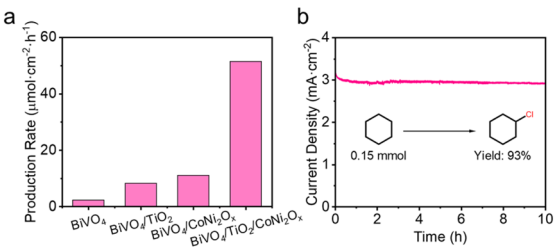

Fig. 3 (a) Production rate of chlorocyclohexane from the C–H chlorination of cyclohexane. Reaction time: 2 h (30 mL NaCl electrolyte, 2 mL cyclohexane, 0.8 V *vs.* RHE, Ar atmosphere). (b) The *J*–t curve for the chlorination of 0.15 mmol cyclohexane and the yield of chlorocyclohexane at 0.8 V *vs.* RHE under an Ar atmosphere. Reaction time: 10 h.

Table 1 PEC chlorination of hydrocarbons over $BiVO_4/TiO_2/CoNi_2O_x$ photoanode in Ar[a]

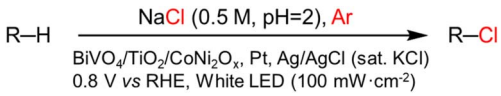

Entry	Substrate	Chlorinated product	FE_{main}[b]
1			93%
2		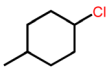	96%
3			82%
4		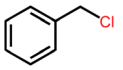	84%
5	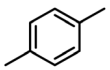	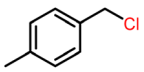	83%
6	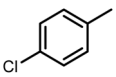	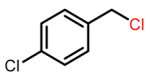	67%
7	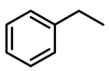	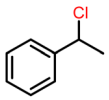	90%
8	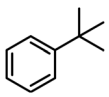	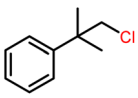	33%

[a] Reaction conditions: 30 mL 0.5 M NaCl (pH = 2) solution, 1–2 mL hydrocarbons, white LED (100 mW cm^{-2}), 1 atm Ar. [b] FE of main chlorinated products was determined by NMR, GC and GC-MS.

A wider scope of substrates was then tested to further establish the general applicability of PEC chlorination of C(sp^3)–H bonds over the $BiVO_4/TiO_2/CoNi_2O_x$ photoanode (Table 1). For the chlorination of cycloheptane, 4-chloro-1-methylcyclohexane was the primary product, likely due to a carbon radical rearrangement (Table 1, entry 2). We then investigated the site selectivity of the chlorination using methylcyclohexane as the substrate (Table 1, entry 3). Chlorination predominantly occurred at the secondary C–H bond, with minimal primary chlorination and no tertiary chlorination detected *via* gas chromatography-mass spectrometry (GC-MS)

analysis. This high selectivity for secondary C–H chlorination is consistent with previously reported site-selective aliphatic C–H chlorination using *N*-chloroamides and visible light.[60]

To gain insight into the active species driving chlorination, we analyzed the chlorinated products of toluene and its derivatives, because toluene contains both active benzyl C(sp^3)–H bonds and aryl C(sp^2)–H bonds. Benzyl chloride was the predominant product, with only trace amounts of phenyl chloride, indicating that chlorination was driven by Cl˙ radical-mediated HAT rather than electrophilic aromatic substitution by Cl_2 (Table 1, entry 4). Substrates prone to oxidation, such as toluene, were not directly oxidized at the electrode interface in the aqueous solution, but instead mediated by Cl˙ in the organic phase due to the insolubility of organic substrates in NaCl aqueous solution in the PEC cell. This approach demonstrated an excellent product selectivity. Electron-donating (Table 1, entry 5) and electron-withdrawing groups (Table 1, entry 6) had minimal influence on selectivity. However, the chlorination of 4-chlorotoluene yielded a lower FE, likely due to its higher BDE. Similarly, for ethylbenzene, the reaction selectively produced (1-chloroethyl)benzene, because secondary C–H bonds are weaker than primary bonds (Table 1, entry 7). Chlorination of *tert*-butylbenzene yielded neophyl chloride as the main product, despite the increased inertness of alkyl C(sp^3)–H bonds compared to toluene (Table 1, entry 8).

Interestingly, alicyclic hydrocarbons such as cyclohexane demonstrate higher FE compared to aromatic hydrocarbons, despite their higher BDE. We tentatively attribute this to the variable absorption properties of Cl_2 in different solvents. As shown in Fig. S21, there is a red-shift of Cl_2 absorption spectra in cyclohexane compared to 0.5 M NaCl (pH = 2) aqueous solution, while a blue-shift is observed in toluene and similar aromatic hydrocarbons. This enables Cl_2 to be more easily excited by visible light in alicyclic hydrocarbons, whereas in aromatic hydrocarbons such as toluene, there is less absorption of visible light and therefore less efficient generation of Cl˙, resulting in lower FE. However, it should be noted that FE does not equate to product selectivity. The selectivity for chlorinated products remained consistently above 90%, as evidenced by GC and NMR analyses which revealed only negligible amounts of byproducts. Overall, the PEC chlorination results suggest that C–H chlorination over $BiVO_4/TiO_2/CoNi_2O_x$ photoanode was primarily driven by Cl˙.[27]

Mechanistic investigation of C(sp^3)–H activation

To determine whether Cl˙ serves as the HAT agent driving the C–H chlorination, we first investigated the possible reaction of Cl_2 and cyclohexane in the dark. As shown in Fig. 4a, only trace amounts of chlorocyclohexane were detected. However, when Cl_2 was exposed to AM 1.5G light or AM 1.5G light coupled with a long-pass filter (λ > 405 nm), the production of chlorocyclohexane increased significantly (Fig. 4a). These results suggest that the CER product, Cl_2, is insufficient to activate C–H bonds directly and that light excitation is needed to generate reactive intermediates, such as Cl˙, to drive C–H chlorination.[61]

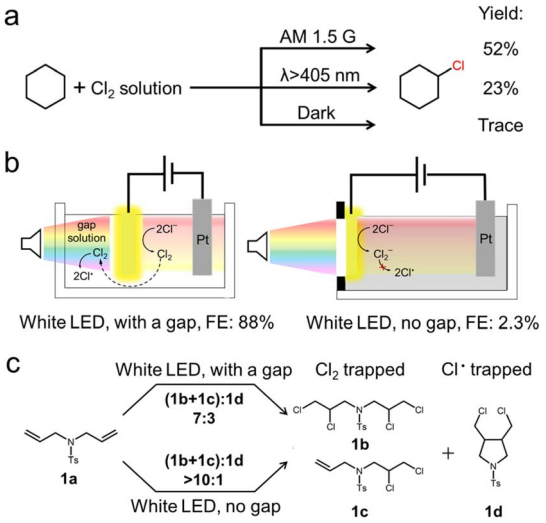

Fig. 4 (a) Chlorocyclohexane yield for cyclohexane chlorination at indicated illumination conditions. (b) Schematic illustration for the control trials of PEC chlorination. Left: gap between the photoanode and the inner wall of the cell, allowing Cl_2 to absorb blue photons; right: no gap, Cl_2 could not absorb blue photons. (c) Selectivity of chlorinated products of diene **1a** with different setups: with a gap or no gap.

Next, we conducted PEC C–H chlorination in the presence of various scavengers. The addition of the radical scavenger 2,2,6,6-tetramethylpiperidinyl-1-oxide (TEMPO) and the hole scavenger ammonium oxalate (AO) completely suppressed the formation of chlorocyclohexane (Fig. S27). This result indicates that both radicals and holes are involved in the reaction, further confirming the role of Cl˙ as the active species. Based on these findings, two possible pathways for C–H chlorination with the $BiVO_4/TiO_2/CoNi_2O_x$ photoanode were proposed: (1) Cl˙ is directly generated on the photoanode surface and quickly reacts with cyclohexane before Cl_2 evolves, or (2) Cl_2 is first evolved from the photoanode, and then Cl˙ is produced *via* light excitation.

To distinguish between these two pathways, we measured the FE of chlorocyclohexane production with different PEC cell configurations (Fig. 4b). In the first setup, a gap between the photoanode and the inner wall of the PEC cell allowed Cl_2 to diffuse and absorb blue photons from the light source, and the $BiVO_4/TiO_2/CoNi_2O_x$ photoanode exhibited a high FE of 88% for chlorocyclohexane production (Fig. 4b, left). In the second setup, the photoanode was placed directly against the inner wall, preventing Cl_2 from being excited by the incident light (which was mostly absorbed by $BiVO_4$), and the FE dropped significantly to 2.3% (Fig. 4b, right). These results confirm that the excitation of Cl_2 to form Cl˙ is crucial for driving C–H bond activation (the second pathway). This mechanism was further supported by a trapping experiment using a diene substrate (**1a**), which produced distinct chlorination products that depend on whether Cl_2 (**1b** & **1c**) or Cl˙ (**1d**) was the active species.[62] The amount of **1d** was found to decrease greatly when the photoanode was in the second setup (Fig. S28 and 4c). In addition, when there was no E_{app} or when inert SO_4^{2-} was

present instead of Cl^-, no chlorocyclohexane was detected, indicating that the PEC process, which oxidizes Cl^- to produce Cl_2, is essential for the overall chlorination reaction. Overall, control experiments were conducted to separate the photocatalysis (PC) step and the PEC step to illustrate their individual roles in our two-step coupled system (Table S4). We found that the PEC process efficiently generates Cl_2 at a lower E_{app}, while the PC process excites Cl_2 to produce $Cl^\bullet$, initiating the C–H chlorination reaction. Both of the two steps are essential, with the PEC step first and the PC step second in a coupled manner.

We also investigated the effect on the FE of chlorocyclohexane production of varying the irradiation wavelengths with appropriate combinations of long-pass and short-pass filters (see Experimental section). Under the same conditions, the FE for chlorinated products as a function of wavelength directly correlates with the absorptance of Cl_2 (Fig. S12a). The external quantum efficiency (EQE), which represents the number of product molecules produced per incident photon,[63,64] also aligns with the FE trend (Fig. S12b). This also confirms that the excitation of Cl_2 is the key step in generating $Cl^\bullet$, which then initiates the C–H chlorination reaction.

Because of the existence of an association equilibrium for the formation of $Cl_2^{\bullet-}$ when $Cl^\bullet$ is photogenerated (eqn (2), $K_{eq} \sim 1.4 \times 10^5$ M^{-1}),[47,65,66] $Cl_2^{\bullet-}$ is a possible alternative reactive intermediate for activation of C(sp^3)–H bonds, as was observed in a prior report.[67]

$$Cl^\bullet + Cl^- \rightleftharpoons Cl_2^{\bullet-} \quad (2)$$

To elucidate the distinct roles of $Cl^\bullet$ and $Cl_2^{\bullet-}$ species in the reaction system, TA measurements were conducted in 0.5 M NaCl aqueous solution containing Cl_2. Upon photoexcitation of Cl_2, a positive absorption signal spanning 300–450 nm was observed (Fig. 5a). The characteristic absorption peak at 340 nm corresponds to $Cl_2^{\bullet-}$,[67] while the weaker $Cl^\bullet$ signal at 320 nm arises from two factors: (1) partial spectral overlap between these species, and (2) competing ground-state bleaching of Cl_2 at 320 nm, which superimposes with and obscures the $Cl^\bullet$ transient signal. The $Cl_2^{\bullet-}$ species exhibits a characteristic lifetime of 4.5 μs at 340 nm. However, the addition of cyclohexane to this solution did not alter the kinetics of $Cl_2^{\bullet-}$ (Fig. 5b), suggesting that $Cl_2^{\bullet-}$ is not a sufficiently potent oxidant to activate the cyclohexane C–H bond. This observation aligns with previous estimates of the redox potential difference between $Cl_2^{\bullet-}/Cl^-$ and $Cl^\bullet/Cl^-$, which indicates that $Cl_2^{\bullet-}$ is a weaker oxidant than $Cl^\bullet$.[68] Although this result is contrary to a previous work by Wu, *et al.*,[49] the observed differences between our study and this earlier work likely arise from the differing reaction conditions, including pH values, aqueous/organic phase ratios (10 : 1 *vs.* 1 : 4), and $Cl^\bullet$ generation methods, which collectively influence the concentration of $Cl_2^{\bullet-}$ species and product selectivity.

The earlier work achieved exceptional product selectivity through a biphasic system where $Cl^\bullet$ and $Cl_2^{\bullet-}$ are generated in the aqueous phase.[49] By removing the possibility of direct contact between the short-lived $Cl^\bullet$ and the organic substrates, only $Cl_2^{\bullet-}$ (with a microsecond lifetime) is sufficiently long-lived

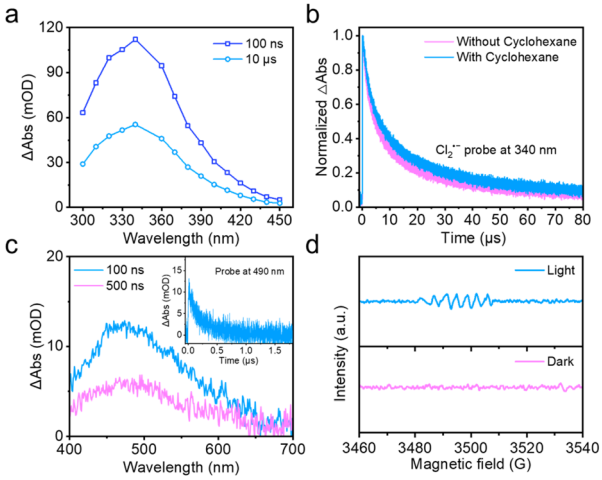

Fig. 5 (a) Transient absorption spectra of $Cl^\bullet$ and $Cl_2^{\bullet-}$ measured at indicated time delays in 0.5 M NaCl (pH = 2) aqueous solution (λ_{ex} = 355 nm, 4 mJ per pulse). (b) Normalized transient kinetic TA spectral data with 0.5 M NaCl (pH = 2) containing Cl_2 at 340 nm, with or without cyclohexane (λ_{ex} = 355 nm, 10 mJ per pulse). (c) Transient absorption spectra of the $Cl^\bullet$-arene adduct measured at indicated time delays in 0.5 M NaCl (pH = 2) aqueous solution containing 1 mL toluene and photoelectrochemically generated Cl_2 under the *operando* condition (λ_{ex} = 355 nm, 4 mJ per pulse). Insert: transient kinetic data for the $Cl^\bullet$-arene adduct monitored at a probe wavelength of 490 nm. (d) ESR detection of $Cl^\bullet$ formation in the two-step coupled PEC system using DMPO as spin-trapping agent under the indicated light or dark conditions.

to diffuse into the organic phase and drive reactions. In our present system, stable Cl_2—rather than transiently lived intermediates—is initially generated by the PEC method, and then diffuses into the organic phase, where it undergoes photolysis to produce $Cl^\bullet$ that reacts immediately with the substrates. While minor contributions from $Cl_2^{\bullet-}$-mediated pathways cannot be entirely ruled out for substrates with lower oxidation potential (such as toluene), two factors strongly favor $Cl^\bullet$-dominated reactivity. Firstly, the extremely low solubility of NaCl in the organic phase severely limits $Cl_2^{\bullet-}$ formation. Secondly, the rapid generation of $Cl^\bullet$ in the organic phase, coupled with its significantly higher reaction rate with toluene ($Cl^\bullet$, $k = 10^{10}$ M^{-1} s^{-1})[69] compared to $Cl_2^{\bullet-}$ ($Cl_2^{\bullet-}$, $k \leq 10^6$ M^{-1} s^{-1}),[70] ensures that even if trace amounts of $Cl_2^{\bullet-}$ diffuse into the organic phase from the aqueous phase, the $Cl_2^{\bullet-}$ reactivity remains orders of magnitude slower. We therefore conclude that $Cl^\bullet$ is the dominant reactive species in this reaction.

Due to the difficulty in observing the TA signals of $Cl^\bullet$, we turned to observing the transient signals of the complex between $Cl^\bullet$ and arene. The TA experiment was conducted under *operando* conditions where Cl_2 is generated from 0.5 M NaCl (pH = 2) aqueous solution in an operating PEC cell. The solution also contained 1 mL of toluene for the detection of transient $Cl^\bullet$. The characteristic transient absorption signal of the $Cl^\bullet$-arene adducts (which subsequently form stable chlorinated products[70–72]) was observed between 400 and 700 nm upon 355 nm pulsed laser excitation, with a lifetime of about 0.24 μs (Fig. 5c).[73,74] This result confirms the photogeneration of

Cl˙ from Cl_2 excitation, and demonstrates the intrinsic reactivity potential of toluene and Cl˙. To further confirm this, ESR measurements were carried out to detect possible radicals. 5,5-Dimethyl-1-pyrroline *N*-oxide (DMPO) was used as the spin-trapping reagent to capture the possible radicals generated after the secondary excitation in the two-step coupled system under the experimental conditions. As shown in Fig. 5d, a seven-line ESR spectrum corresponding to DMPOX[75–78] was observed after irradiation, directly indicating the photogeneration of Cl˙ under the secondary light excitation. Recently, Qiu's group[79] published a study on photoelectrocatalytic Cl˙-mediated C(sp^3)–H aminomethylation of hydrocarbons by $BiVO_4$ photoanodes, which also highlighted the generation of Cl˙ from Cl_2 homolysis, though they employed Me_4NCl as the chlorine source in purely organic solution. In contrast, our work utilizes a more cost-effective and readily available NaCl aqueous solution as the chloride source. The hydrogen atom transfer reaction, initiated by Cl˙ from Cl_2 homolysis, occurs in the organic phase—requiring prior diffusion of stable Cl_2 across the aqueous–organic interface. This spatial separation between the photoelectrode interface and the hydrocarbon substrates, which are prone to direct oxidation, potentially minimizes overoxidation and improves faradaic efficiency. Recently, two additional studies on PEC C–H bonds chlorination have emerged,[43,80] which complement our work both mechanistically and performance-wise, collectively underscoring the significance of PEC chlorine radical generation.

Table 2 PEC oxidation of arene over $BiVO_4/TiO_2/CoNi_2O_x$ photoanode in O_2[a]

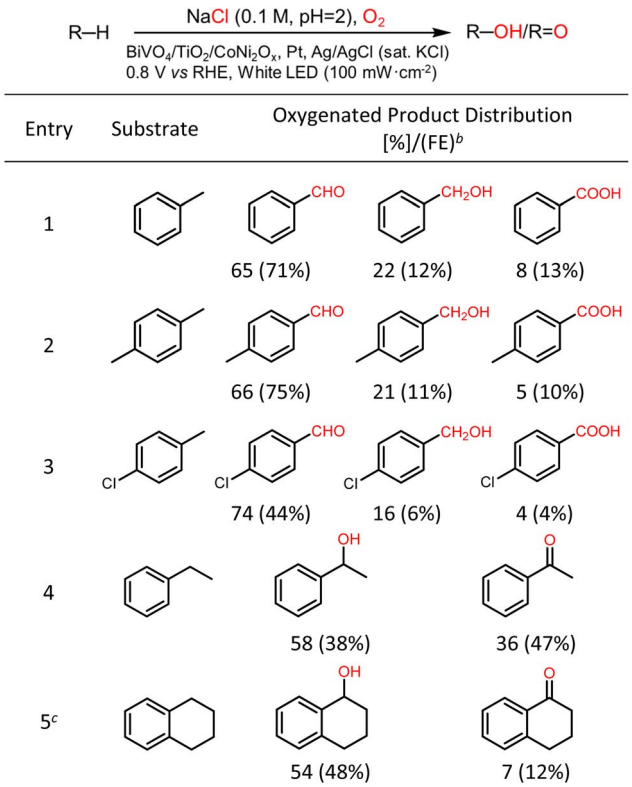

[a] Reaction conditions: 20 mL 0.1 M NaCl (pH = 2) solution, 4 mL arene, white LED (100 mW cm^{-2}), 1 atm O_2. [b] FE and selectivities of oxygenated products were determined by GC and NMR. [c] Besides alcohol (54%) and ketone (7%), chlorinated products with 39% selectivity were detected.

Photoelectrochemical oxygenation of C(sp^3)–H bonds

The generation of carbon radicals *via* Cl˙-mediated C–H activation opens the possibility of direct oxygenation of C–H bonds using molecular O_2. Compared to traditional oxidants such as hypervalent iodine,[81] S_2O_8 (ref. 2–7) and chromium(VI) salts,[82] which are often toxic, expensive, and environmentally hazardous, molecular O_2 offers a more sustainable and cost-effective alternative with high atom utilization efficiency. Leveraging our strategy for Cl˙ generation through the PEC process, aldehydes, ketones, and alcohols were produced as oxygenated products under an O_2 atmosphere, with minimal formation of chlorinated byproducts (Table 2).

Toluene was selected as the model substrate for the oxidation of C–H bonds (Table 2, entry 1, Fig. S22). The primary products were benzaldehyde and benzyl alcohol, with selectivities of 65% and 22%, respectively, and only small amounts of benzoic acid (8%) and chlorinated products (less than 5%). The FE for the main oxygenated product, benzaldehyde, was approximately 71%. It is likely that benzyl alcohol serves as an intermediate oxygenated product in the PEC oxygenation process; however, due to the excess of toluene, the system appears to reach an equilibrium between benzyl alcohol and benzaldehyde. The alicyclic hydrocarbon cyclohexane was also tested as a substrate but it showed much lower selectivity and hence is not listed.

The substrate scope was subsequently explored with a range of aromatic compounds. As observed in the chlorination reactions, electron-donating (Table 2, entry 2) and electron-withdrawing groups (Table 2, entry 3) did not significantly affect the product selectivity, although 4-chlorotoluene exhibited a lower FE (44% for aldehyde formation) due to its higher BDE. Ethylbenzene, which contains weaker secondary C–H bonds, showed higher selectivity for 1-phenylethanol (58%) compared to acetophenone (36%) with a good overall FE (Table 2, entry 4). This outcome is likely due to the preferential formation of alcohols from the more reactive secondary C–H bond, with ketones forming more slowly. Tetralin, on the other hand, displayed lower selectivity for oxygenated products, with 55% selectivity for alcohols, 8% for ketones, and a significant proportion of chlorinated byproducts (39%). This suggests that electrophilic aromatic substitution by Cl_2 competes with the oxygenation process (Table 2, entry 5). These results highlight the potential of Cl˙ in facilitating selective C(sp^3)–H bond oxidation under mild conditions, offering a sustainable and efficient approach to oxygenating aromatic hydrocarbons using molecular O_2 in PEC cells.

To determine whether the active species in the oxygenation reaction are Cl˙ and molecular O_2 rather than superoxide radical ($O_2^{\cdot-}$) or singlet oxygen ($^1O_2$), we conducted detection

and quenching experiments. We used 9,10-anthracenediylbis(-methylene)dimalonic acid (ABDA)[83] to detect $^1O_2$ (Fig. S30a). The absorption of ABDA showed no significant decrease, confirming the absence of $^1O_2$. Additionally, $^1O_2$ is typically formed *via* triplet energy transfer from a triplet excited state photosensitizer, which was absent in our system.[84] Dihydrorhodamine 123 (DHR123) was used as a fluorescent probe to detect $O_2^{\bullet-}$.[85] No significant fluorescence was observed at 550 nm during the reaction, indicating the absence of $O_2^{\bullet-}$ (Fig. S30b). Furthermore, quenching $O_2^{\bullet-}$ with 1,4-benzoquinone (BQ) resulted in only minor changes in selectivity and FE of the oxygenation products, possibly due to BQ interfering with Cl_2 absorption rather than quenching a reactive intermediate. When a long-pass filter (λ > 405 nm) was used to suppress Cl$^\bullet$ formation, a marked decrease in the FE of the oxygenated products was observed (Fig. S30c), indicating that chlorine radicals are the key active species.

To unambiguously identify the oxygen source, we conducted $H_2{}^{18}O$ isotope labeling experiments and analyzed the products *via* GC-MS (Fig. S31). The results revealed negligible incorporation of ^{18}O into benzaldehyde under $H_2{}^{18}O$ conditions, confirming that the oxygen in the product does not originate from water. The minor presence of ^{18}O-labeled benzaldehyde likely arose from PEC-generated oxygen at the photoanode, consistent with the minor O_2 byproducts observed in Fig. 2e and parallel chlorination experiments. Moreover, by simply changing the reaction atmosphere from Ar to O_2, without altering other parameters, we observed a complete transition from chlorinated products to exclusively oxygenated products. If water had been the primary source, oxygenation products should have appeared, even under the Ar atmosphere. However, control experiments under Ar conditions showed exclusive formation of chlorinated products, further reinforcing O_2 as the dominant oxygen source in our system. Combining these results with the absence of oxygenation products under Ar conditions, we conclude that the active species in the oxygenation reaction are Cl$^\bullet$ and molecular O_2.

Scheme 2 summarizes the photoelectrochemical chlorination and oxygenation of C(sp^3)–H bonds under either inert or oxygen environment, driven by the generation of Cl$^\bullet$ as the key HAT intermediate. The process begins with the efficient generation of Cl_2 through photoelectrochemical oxidation of Cl^- in the NaCl aqueous solution following the absorption of the first photon on the $BiVO_4/TiO_2/CoNi_2O_x$ photoanode (blue arrow). Subsequently, the stable Cl_2 diffuses into the organic phase, where it undergoes photoexcitation (light red arrow) to form Cl$^\bullet$, which serves as the HAT agent, abstracting a hydrogen atom from the C(sp^3)–H bond and generating a carbon-centered radical. This radical then reacts with chlorine species or molecular O_2, completing the chlorination or oxygenation of the C–H bonds (Fig. S32). This two-step coupled photoexcitation process in the PEC cell effectively accumulates free energy, allowing the system to circumvent the high reduction potential ($E°$(Cl$^\bullet$/Cl$^-$)) and generate the reactive Cl$^\bullet$ intermediate, enabling efficient C(sp^3)–H activation at a low applied bias.

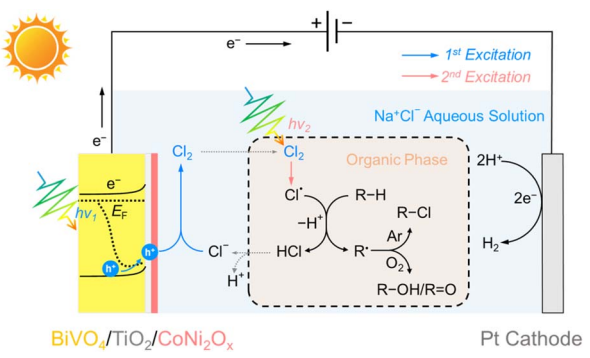

Scheme 2 Schematic illustration of the two-step coupled PEC C–H activation process. E_F is the quasi-Fermi level of the photoanode.

Conclusions

In conclusion, we have developed a high-performance $BiVO_4/TiO_2/CoNi_2O_x$ photoanode for photoelectrochemical C(sp^3)–H bond functionalization through a novel two-step coupled process. This approach leverages the PEC-driven chlorine radical (Cl$^\bullet$) generation to achieve both chlorination and oxygenation of hydrocarbons in a facile and sustainable way. The photoanode first demonstrates excellent Cl_2 evolution efficiency with a photocurrent density of 2.9 mA cm^{-2} at a low applied bias of 0.8 V *vs.* RHE, approximately 0.7 V lower than that required for direct electrochemical oxidation of chlorides. The low applied bias brings the advantage of net energy output rather than net energy consumption, achieving a positive applied bias photon-to-current efficiency (ABPE) of up to 3.20%. In the second step of the two-step coupled process, the evolved Cl_2 is subsequently photolyzed to form Cl$^\bullet$, which is responsible for C(sp^3)–H bond activation. Compared to chlorination reaction by direct excitation of chlorine gas which is usually hazardous, we avoided the direct use of hazardous Cl_2 and external expensive oxidants, achieving chlorination reactions directly from Cl^- which is cheaper, easier accessible, and nontoxic.

Mechanistic studies revealed that Cl$^\bullet$ is the key intermediate responsible for initiating C–H bond activation, as confirmed by transient absorption spectroscopy, electron spin resonance and controlled experiments with scavengers. Selective chlorination of aliphatic and aromatic hydrocarbons was achieved under mild conditions with high faradaic efficiency. The system exhibited good selectivity when mediated by Cl$^\bullet$ rather than Cl_2 or $Cl_2^{\bullet-}$. Additionally, under O_2 conditions, Cl$^\bullet$ facilitated the oxygenation of C–H bonds, producing aldehydes, ketones, and alcohols in an environmentally friendly and sustainable manner using molecular O_2. This study offers a promising strategy for advancing solar-driven fine chemical synthesis, providing an efficient route to value-added products from simple hydrocarbons. The low applied bias and high atom utilization efficiency make this approach a sustainable alternative to traditional methods, demonstrating the potential for broader applications in solar-driven energy-demanding synthesis.

Author contributions

W. Yang and Y. Han synthesized the materials. W. Yang and P. Li performed the experiments. W. Yang and Y. Han wrote the manuscript. Z. Zhao, L. Tian and M. G. Humphrey modified the figures and the manuscript. Z. Zhang and Y. Han contributed to the characterizations. K. Hu and C. Zhang conceptualised and supervised the research and contributed to reviewing and editing the manuscript. All authors discussed the results and contributed to the final manuscript.

Conflicts of interest

There are no conflicts to declare.

Data availability

Supplementary information: detailed materials and methods; SEM, HRTEM, XRD, XPS spectra; IMPS, EIS, ABPE and LSV curves; NMR, GC and GC-MS spectra. See DOI: **https://doi.org/10.1039/d5sc05195a**.

Acknowledgements

This study is sponsored by National Key R&D Program of China (2023YFE0124100), National Natural Science Foundation of China (22173022), Fundamental Research Funds for the Central Universities, and the China Postdoctoral Science Foundation (2025T180305, 2024M760508, GZB20240159).

Notes and references

1 D. I. Enache, J. K. Edwards, P. Landon, B. Solsona-Espriu, A. F. Carley, A. A. Herzing, M. Watanabe, C. J. Kiely, D. W. Knight and G. J. Hutchings, *Science*, 2006, **311**, 362–365.
2 X. Cao, Z. Chen, R. Lin, W.-C. Cheong, S. Liu, J. Zhang, Q. Peng, C. Chen, T. Han, X. Tong, Y. Wang, R. Shen, W. Zhu, D. Wang and Y. Li, *Nat. Catal.*, 2018, **1**, 704–710.
3 R. G. Bergman, *Nature*, 2007, **446**, 391–393.
4 D. Cantillo, *Curr. Opin. Electrochem.*, 2024, **44**, 101459.
5 P. S. Baran and Y.-L. Zhong, *J. Am. Chem. Soc.*, 2001, **123**, 3183–3185.
6 Z. Zhang, X. Song, G. Li, X. Li, D. Zheng, X. Zhao, H. Miao, G. Zhang and L. Liu, *Chin. Chem. Lett.*, 2021, **32**, 1423–1426.
7 C. Huang, J.-H. Wang, J. Qiao, X.-W. Fan, B. Chen, C.-H. Tung and L.-Z. Wu, *J. Org. Chem.*, 2019, **84**, 12904–12912.
8 L. Ding, J. Tang, M. Cui, C. Bo, X. Chen and X. Qiao, *Ind. Eng. Chem. Res.*, 2011, **50**, 11143–11152.
9 S. M. Maddox, C. J. Nalbandian, D. E. Smith and J. L. Gustafson, *Org. Lett.*, 2015, **17**, 1042–1045.
10 S. Song, X. Li, J. Wei, W. Wang, Y. Zhang, L. Ai, Y. Zhu, X. Shi, X. Zhang and N. Jiao, *Nat. Catal.*, 2020, **3**, 107–115.
11 W. Liu and J. T. Groves, *J. Am. Chem. Soc.*, 2010, **132**, 12847–12849.
12 L. Kesavan, R. Tiruvalam, M. H. A. Rahim, M. I. bin Saiman, D. I. Enache, R. L. Jenkins, N. Dimitratos, J. A. Lopez-Sanchez, S. H. Taylor, D. W. Knight, C. J. Kiely and G. J. Hutchings, *Science*, 2011, **331**, 195–199.
13 A. K. Cook, S. D. Schimler, A. J. Matzger and M. S. Sanford, *Science*, 2016, **351**, 1421–1424.
14 R. A. Periana, O. Mironov, D. Taube, G. Bhalla and C. J. Jones, *Science*, 2003, **301**, 814–818.
15 X. Yang, Q.-L. Yang, X.-Y. Wang, H.-H. Xu, T.-S. Mei, Y. Huang and P. Fang, *J. Org. Chem.*, 2020, **85**, 3497–3507.
16 Y.-C. Wu, R.-J. Song and J.-H. Li, *Org. Chem. Front.*, 2020, **7**, 1895–1902.
17 L. Buglioni, F. Raymenants, A. Slattery, S. D. A. Zondag and T. Noël, *Chem. Rev.*, 2022, **122**, 2752–2906.
18 L. Qian and M. Shi, *Chem. Commun.*, 2023, **59**, 3487–3506.
19 D. M. Schultz and T. P. Yoon, *Science*, 2014, **343**, 1239176.
20 Y.-J. Chen, T. Lei, H.-L. Hu, H.-L. Wu, S. Zhou, X.-B. Li, B. Chen, C.-H. Tung and L.-Z. Wu, *Matter*, 2021, **4**, 2354–2366.
21 J. P. Barham and B. König, *Angew. Chem., Int. Ed.*, 2020, **59**, 11732–11747.
22 T. Tong, M. Zhang, W. Chen, X. Huo, F. Xu, H. Yan, C. Lai, W. Wang, S. Hu, L. Qin and D. Huang, *Coord. Chem. Rev.*, 2024, **500**, 215498.
23 L. Zhang, L. Liardet, J. Luo, D. Ren, M. Grätzel and X. Hu, *Nat. Catal.*, 2019, **2**, 366–373.
24 T. Li, T. Kasahara, J. He, K. E. Dettelbach, G. M. Sammis and C. P. Berlinguette, *Nat. Commun.*, 2017, **8**, 390.
25 H. Tateno, S. Iguchi, Y. Miseki and K. Sayama, *Angew. Chem., Int. Ed.*, 2018, **57**, 11238–11241.
26 J.-H. Wang, X.-B. Li, J. Li, T. Lei, H.-L. Wu, X.-L. Nan, C.-H. Tung and L.-Z. Wu, *Chem. Commun.*, 2019, **55**, 10376–10379.
27 Z. Li, L. Luo, M. Li, W. Chen, Y. Liu, J. Yang, S.-M. Xu, H. Zhou, L. Ma, M. Xu, X. Kong and H. Duan, *Nat. Commun.*, 2021, **12**, 6698.
28 Y. He, Z. Huang, K. Wu, J. Ma, Y.-G. Zhou and Z. Yu, *Chem. Soc. Rev.*, 2022, **51**, 2759–2852.
29 S. K. Kariofillis and A. G. Doyle, *Acc. Chem. Res.*, 2021, **54**, 988–1000.
30 Z. Chen, M.-Y. Rong, J. Nie, X.-F. Zhu, B.-F. Shi and J.-A. Ma, *Chem. Soc. Rev.*, 2019, **48**, 4921–4942.
31 Z. Yang, W. Shi, H. Alhumade, H. Yi and A. Lei, *Nat. Synth.*, 2023, **2**, 217–230.
32 Y. Kawamata, M. Yan, Z. Liu, D.-H. Bao, J. Chen, J. T. Starr and P. S. Baran, *J. Am. Chem. Soc.*, 2017, **139**, 7448–7451.
33 F. Wang and S. S. Stahl, *Acc. Chem. Res.*, 2020, **53**, 561–574.
34 H. Gao, Z. Zha, Z. Zhang, H. Ma and Z. Wang, *Chem. Commun.*, 2014, **50**, 5034–5036.
35 E. J. Horn, B. R. Rosen, Y. Chen, J. Tang, K. Chen, M. D. Eastgate and P. S. Baran, *Nature*, 2016, **533**, 77–81.
36 L. Niu, C. Jiang, Y. Liang, D. Liu, F. Bu, R. Shi, H. Chen, A. D. Chowdhury and A. Lei, *J. Am. Chem. Soc.*, 2020, **142**, 17693–17702.
37 H. Huang, Z. M. Strater and T. H. Lambert, *J. Am. Chem. Soc.*, 2020, **142**, 1698–1703.
38 L. Zhang, Y. Fu, Y. Shen, C. Liu, M. Sun, R. Cheng, W. Zhu, X. Qian, Y. Ma and J. Ye, *Nat. Commun.*, 2022, **13**, 4138.

39 D. E. Essayan, M. J. Schubach, J. M. Smoot, T. Puri and S. V. Pronin, *J. Am. Chem. Soc.*, 2024, **146**, 18224–18229.
40 C. Yang, L. A. Farmer, E. C. McFee, R. K. Jha, S. Maldonado, D. A. Pratt and C. R. J. Stephenson, *Angew. Chem., Int. Ed.*, 2024, **63**, e202315917.
41 S. Han, C. Cheng, M. He, R. Li, Y. Gao, Y. Yu, B. Zhang and C. Liu, *Angew. Chem., Int. Ed.*, 2023, **62**, e202216581.
42 G.-X. Dong, M.-R. Zhang, S.-X. Yuan, M. Zhang and T.-B. Lu, *Angew. Chem., Int. Ed.*, 2025, **64**, e202510993.
43 Y. Tao, J. Ding, Z. Teng, Q. Xu, W. Ou, H. Sun, S. Li, L. Yu, G. Li, B. Liu and C. Su, *J. Am. Chem. Soc.*, 2025, **147**, 18814–18825.
44 Q. Yang, Y.-H. Wang, Y. Qiao, M. Gau, P. J. Carroll, P. J. Walsh and E. J. Schelter, *Science*, 2021, **372**, 847–852.
45 M. I. Gonzalez, D. Gygi, Y. Qin, Q. Zhu, E. J. Johnson, Y.-S. Chen and D. G. Nocera, *J. Am. Chem. Soc.*, 2022, **144**, 1464–1472.
46 T. Liang, Z. Lyu, Y. Wang, W. Zhao, R. Sang, G.-J. Cheng and F. Ye, *Nat. Chem.*, 2025, **17**, 598–605.
47 L. Troian-Gautier, M. D. Turlington, S. A. M. Wehlin, A. B. Maurer, M. D. Brady, W. B. Swords and G. J. Meyer, *Chem. Rev.*, 2019, **119**, 4628–4683.
48 W. Li, J. Liu, M. Zhou, L. Ma and M. Zhang, *Org. Biomol. Chem.*, 2022, **20**, 6667–6672.
49 Q. Zhang, B. An, Y. Lei, Z. Gao, H. Zhang, S. Xue, X. Jin, W. Xu, Z. Wu, M. Wu, X. Yang and W. Wu, *Angew. Chem., Int. Ed.*, 2023, **62**, e202304699.
50 R. Sun, Z. Zhu, N. Tian, Y. Zhang and H. Huang, *Angew. Chem., Int. Ed.*, 2024, **63**, e202408862.
51 H. Wang, Z. Chen, Y. Shang, C. Lv, X. Zhang, F. Li, Q. Huang, X. Liu, W. Liu, L. Zhao, L. Ye, H. Xie and X. Jin, *ACS Catal.*, 2024, **14**, 5779–5787.
52 T. W. Kim and K.-S. Choi, *Science*, 2014, **343**, 990–994.
53 D. Liu, J.-C. Liu, W. Cai, J. Ma, H. B. Yang, H. Xiao, J. Li, Y. Xiong, Y. Huang and B. Liu, *Nat. Commun.*, 2019, **10**, 1779.
54 E. Usman, M. Barzgar Vishlaghi, A. Kahraman, N. Solati and S. Kaya, *ACS Appl. Mater. Interfaces*, 2021, **13**, 60602–60611.
55 Q. Wang, T. Li, C. Yang, M. Chen, A. Guan, L. Yang, S. Li, X. Lv, Y. Wang and G. Zheng, *Angew. Chem., Int. Ed.*, 2021, **60**, 17398–17403.
56 C. Zachäus, F. F. Abdi, L. M. Peter and R. van de Krol, *Chem. Sci.*, 2017, **8**, 3712–3719.
57 H. Iwami, M. Okamura, M. Kondo and S. Masaoka, *Angew. Chem., Int. Ed.*, 2021, **60**, 5965–5969.
58 M. Kan, D. Xue, A. Jia, X. Qian, D. Yue, J. Jia and Y. Zhao, *Appl. Catal., B*, 2018, **225**, 504–511.
59 Z. Chen, T. F. Jaramillo, T. G. Deutsch, A. Kleiman-Shwarsctein, A. J. Forman, N. Gaillard, R. Garland, K. Takanabe, C. Heske, M. Sunkara, E. W. McFarland, K. Domen, E. L. Miller, J. A. Turner and H. N. Dinh, *J. Mater. Res.*, 2010, **25**, 3–16.
60 R. K. Quinn, Z. A. Könst, S. E. Michalak, Y. Schmidt, A. R. Szklarski, A. R. Flores, S. Nam, D. A. Horne, C. D. Vanderwal and E. J. Alexanian, *J. Am. Chem. Soc.*, 2016, **138**, 696–702.
61 P. Xu, P.-Y. Chen and H.-C. Xu, *Angew. Chem., Int. Ed.*, 2020, **59**, 14275–14280.
62 N. Fu, G. S. Sauer and S. Lin, *J. Am. Chem. Soc.*, 2017, **139**, 15548–15553.
63 G. Zhang, Z.-A. Lan, L. Lin, S. Lin and X. Wang, *Chem. Sci.*, 2016, **7**, 3062–3066.
64 S. Chen, J. Lin, J. Huang, T. Pang, Q. Ye, Y. Zheng, X. Li, Y. Yu, B. Zhuang and D. Chen, *Adv. Funct. Mater.*, 2024, **34**, 2309293.
65 V. Nagarajan and R. W. Fessenden, *J. Phys. Chem.*, 1985, **89**, 2330–2335.
66 X.-Y. Yu and J. R. Barker, *J. Phys. Chem. A*, 2003, **107**, 1313–1324.
67 M. L. Alegre, M. Geronés, J. A. Rosso, S. G. Bertolotti, A. M. Braun, D. O. Mártire and M. C. Gonzalez, *J. Phys. Chem. A*, 2000, **104**, 3117–3125.
68 Y. Lei, S. Cheng, N. Luo, X. Yang and T. An, *Environ. Sci. Technol.*, 2019, **53**, 11170–11182.
69 K. Zhang and K. M. Parker, *Environ. Sci. Technol.*, 2018, **52**, 9579–9594.
70 D. O. Mártire, J. A. Rosso, S. Bertolotti, G. C. Le Roux, A. M. Braun and M. C. Gonzalez, *J. Phys. Chem. A*, 2001, **105**, 5385–5392.
71 M. L. Alegre, M. Geronés, J. A. Rosso, S. G. Bertolotti, A. M. Braun, D. O. Mártire and M. C. Gonzalez, *J. Phys. Chem. A*, 2000, **104**, 3117–3125.
72 Y. Lei, X. Lei, P. Westerhoff, X. Zhang and X. Yang, *Environ. Sci. Technol.*, 2021, **55**, 689–699.
73 Q. An, Y.-Y. Xing, R. Pu, M. Jia, Y. Chen, A. Hu, S.-Q. Zhang, N. Yu, J. Du, Y. Zhang, J. Chen, W. Liu, X. Hong and Z. Zuo, *J. Am. Chem. Soc.*, 2023, **145**, 359–376.
74 S. Förgeteg and T. Bérces, *J. Photochem. Photobiol. A*, 1993, **73**, 187–195.
75 Y. Zhang, J. Li, J. Bai, Z. Shen, L. Li, L. Xia, S. Chen and B. Zhou, *Environ. Sci. Technol.*, 2018, **52**, 1413–1420.
76 R. Song, H. Wang, M. Zhang, Y. Liu, X. Meng, S. Zhai, C.-c. Wang, T. Gong, Y. Wu, X. Jiang and W. Bu, *Angew. Chem., Int. Ed.*, 2020, **59**, 21032–21040.
77 T. Li, Y. Jiang, X. An, H. Liu, C. Hu and J. Qu, *Water Res.*, 2016, **102**, 421–427.
78 L. Wang, J. Guan, H. Han, M. Yao, J. Kang, M. Peng, D. Wang, J. Xu and J. Hao, *Appl. Catal., B*, 2022, **306**, 121130.
79 A. Shi, P. Xie, Y. Wang and Y. Qiu, *Nat. Commun.*, 2025, **16**, 2322.
80 S. Y. Chae, A. Mehmood and E. D. Park, *J. Am. Chem. Soc.*, 2025, **147**, 19472–19477.
81 M. Uyanik, M. Akakura and K. Ishihara, *J. Am. Chem. Soc.*, 2009, **131**, 251–262.
82 A. K. Das, *Coord. Chem. Rev.*, 2004, **248**, 81–99.
83 C. Felip-León, M. Puche, J. F. Miravet, F. Galindo and M. Feliz, *Mater. Lett.*, 2019, **251**, 45–51.
84 Y. Wang, Y. Lin, S. He, S. Wu and C. Yang, *J. Hazard. Mater.*, 2024, **461**, 132538.
85 L. Yu, Y. Xu, Z. Pu, H. Kang, M. Li, J. L. Sessler and J. S. Kim, *J. Am. Chem. Soc.*, 2022, **144**, 11326–11337.